FRONTIERS OF PHYSICS

RESEARCH ARTICLE
Volume 21 / Issue 10 / 102202 / 2026

Sorting and recognition of orbital angular momentum modes through a rotating scattering medium

JinJiang Wang[1], Hongyu Yan[1], Yu Lei[1], Yutian Liang[1], Ruijian Li[1], Tong Liu[1,†], Zhengliang Liu[2], Ziyan Huang[1], Yuan Ren[2,‡]

1 Department of Aerospace Science and Technology, Space Engineering University, Beijing 101416, China
2 Department of Basic Course, Space Engineering University, Beijing 101416, China
Corresponding authors. E-mail: †liutong719@163.com, ‡renyuan_823@aliyun.com
Received January 21, 2026; accepted May 6, 2026

ABSTRACT

Vortex beams carrying orbital angular momentum (OAM) possess infinite-dimensional orthogonal eigenstates, rendering them exceptionally valuable for optical communication and information transmission applications. However, the sorting and recognition of OAM encounter formidable challenges in practical scenarios, especially when propagating through dynamic scattering media. Mode mixing and decoherence induced by time-varying perturbations severely restrict the effective exploitation of OAM. Traditional studies have predominantly focused on the interaction between vortex beams and static scattering media. Even for dynamic scattering media, existing investigations generally rely on synchronous speckle acquisition or deep learning for information retrieval, which inevitably results in complex system configurations or prohibitive computational overheads. To address these issues, this paper proposes an OAM sorting and recognition method for randomly rotating scattering media. By integrating the angularly averaged intensity cross-correlation function with a normalized cross-correlation screening (NCCS) algorithm, we establish a mapping relationship between the topological charge difference and the characteristic features of the cross-correlation ring (CCR). Furthermore, complete sorting and recognition of OAM modes are realized through the dual-reference perfect vortex beam (DRPVB) approach. Experimental results demonstrate that our method successfully overcomes the technical limitations of conventional synchronous speckle acquisition, enabling OAM sorting and recognition under randomly rotating media conditions and thus facilitating the practical application of vortex beams in optical communication and information processing applications.

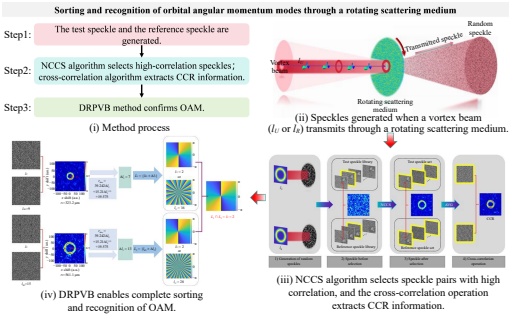

Keywords vortex beam, orbital angular momentum, scattering medium

1 Introduction

With the rapid advancement of optical communication and information transmission technologies, the demand for higher channel capacity and expanded information dimensions has been continuously growing [1, 2]. Vortex beams, by virtue of their unique capability to carry orbital angular momentum (OAM), provide additional degrees of freedom for information encoding and have consequently attracted extensive research attention

https://doi.org/10.15302/frontphys.2026.102202

[3–12]. This stems from the fact that OAM forms an infinite-dimensional set of orthogonal eigenstates in Hilbert space, which theoretically enables the parallel transmission of multiple orthogonal states within a single wavelength channel [13–19]. However, this advantage relies on the accurate sorting and recognition of OAM to achieve effective encoding of multi-dimensional information [20, 21]. Therefore, in-depth research on OAM mode sorting and recognition technologies is of great significance for advancing optical communications and future high-capacity information transmission [22, 23].

In recent years, various methods have been developed for OAM mode recognition, including interferometry [24, 25], spatial mapping [26, 27], multiplane light conversion devices [28–30] and neural networks [31–33], among others. However, most of these methods are only suitable for ideal or controlled optical environments. In practical transmission scenarios, vortex beams are susceptible to scattering by complex media, which causes OAM information to be overwhelmed by speckle noise [34], rendering effective recovery and recognition challenging. To address this issue, researchers have proposed approaches such as transmission matrix inversion [35–39] and deep learning [40–44], which achieve mode recognition by establishing a mapping relationship between the input OAM and the scattered optical field. However, due to practical limitations such as the complexity of transmission matrix calibration and the high computational demands of deep learning, these methods struggle to achieve flexible and efficient application in real scattering media. Notably, in 2012, Kumar *et al.* [45] revealed that intensity fluctuations in speckle are correlated with OAM and angular position, providing a new approach for OAM recognition. In the same year, inspired by this correlation property, Jesus-Silva *et al.* [46] demonstrated the recognition of the topological charge magnitude in static scattering media based on speckle correlation characteristics in 2012, without requiring transmission matrix inversion or deep learning, thus highlighting the potential of speckle correlation in OAM recognition. Subsequently, in 2015, Alves *et al.* [47] utilized the speckle correlation properties obtained with synchronously rotating scattering media to estimate integer-order OAM. Further inspired by polarization characteristics, Vinu and Singh [48] combined polarization measurement with speckle correlation to accomplish the recognition of low-order OAM in static scattering media in 2016. As research progressed, in 2024, Ma *et al.* [49] employed far-field speckle cross-correlation to achieve OAM sorting and demultiplexing under static scattering media. To tackle OAM recognition under dynamic scattering media, Ma *et al.* [50] further integrated polarization characteristics with speckle correlation to enable OAM recognition under dynamic scattering media in 2025, though synchronous acquisition was still required, and only the magnitude of the topological charge could be determined without identifying its sign. In 2025, Ren *et al.* [51] incorporated mainstream deep learning frameworks to achieve OAM recognition under strong turbulence without the need for synchronous acquisition. However, their network structure was relatively complex and generalization capability remained limited. In summary, while speckle correlation methods offer lower computational complexity, they heavily rely on synchronous acquisition of signal and reference beams, imposing stringent requirements on hardware synchronization accuracy and leading to a complex system architecture. Once synchronization fails, the correlation rapidly degrades, resulting in recognition failure [47, 50]. On the other hand, although deep learning avoids synchronous acquisition, if it lacks physical priors on the evolution of dynamic speckles, the algorithm structure becomes overly complex with poor generalization, making it difficult to adapt to complex and dynamic scattering media [51–53].

Therefore, it is imperative to develop a new approach that eliminates the need for precise synchronous calibration and reduces data-processing complexity, thereby facilitating the practical application of vortex beams in dynamic scattering media. To overcome the aforementioned challenges, we propose a method for OAM sorting and recognition in randomly rotating scattering media. This method eliminates the need for both synchronous acquisition and deep learning strategies. It instead employs a normalized cross-correlation screening (NCCS) algorithm to select highly correlated speckles, thereby suppressing dynamic noise and crosstalk from uncorrelated speckles. This approach breaks through the hardware limitations of synchronous acquisition at the data acquisition and preprocessing levels. Furthermore, it utilizes an angular average intensity correlation function to establish a mapping relationship between the topological charge difference (TCD) and the cross-correlation ring (CCR) radius feature. To overcome the limitation that traditional speckle correlation methods can only determine the magnitude of the topological charge but fail to distinguish its sign, we further propose a Dual-reference perfect vortex beam (DRPVB) recognition method. Requiring only two sets of reference perfect vortex beams with different topological charges, this method simultaneously determines both the magnitude and sign of the unknown topological charge, enabling complete OAM mode sorting and recognition. Our proposed method effectively reduces the hardware requirements for speckle acquisition and the data processing complexity, expands the technical pathways for OAM mode sorting and recognition in dynamic scattering media, and advances the practical application of vortex beam communications and information transmission.

2 Concept and principle

To avoid interference from the complex radial structures of traditional Laguerre-Gaussian beams in the measurement of azimuthal OAM spectra, we employed the

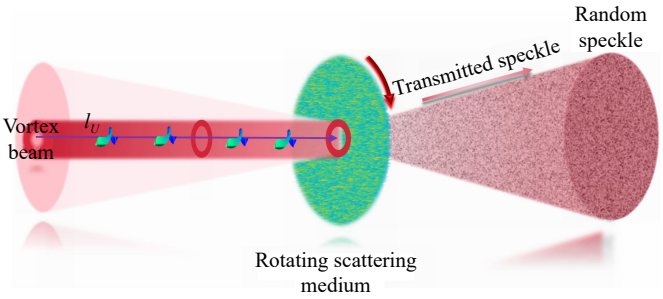

Fig. 1 Schematic diagram of speckles generated when a vortex beam transmits through a rotating scattering medium.

Gaussian apodization method to create a perfect vortex beam (PVB), thereby eliminating the radial degree of freedom and focusing on the precise characterization of azimuthal OAM spectra [49]. The radius of the annular intensity distribution of PVB is independent of the topological charge, The light field of an unknown PVB to be measured can be expressed as [18]

$$\begin{aligned} E_U(r,\theta) &= \exp(-(r_U - r_0)^2/\Delta r^2)\exp(\mathrm{i}l_U\theta_U) \\ &= a_U \exp(\mathrm{i}l_U\theta_U), \end{aligned} \tag{1}$$

where a_U is the field amplitude, l_U is the topological charge, θ_U is the azimuthal angle, r_0 and Δr denote the radius and width of the ring, respectively.

When a vortex beam with topological charge (l_U) propagates through a rotating scattering medium, it generates time-varying speckle patterns, making the OAM information difficult to extract, as shown in Fig. 1.

Meanwhile, we select another PVB as the reference vortex beam (RPVB), which can be expressed as

$$\begin{aligned} E_R(r,\theta) &= \exp(-(r_R - r_0)^2/\Delta r^2)\exp(\mathrm{i}l_R\theta_R) \\ &= a_R \exp(\mathrm{i}l_R\theta_R). \end{aligned} \tag{2}$$

When the unknown PVB under test and RPVB propagate through the same rotating scattering medium, we randomly acquire M and N speckle intensity patterns at different rotation angles, respectively. At this point, the angular average intensity cross-correlation function of the speckle intensity can be expressed as [46]

$$\begin{aligned} &\left\langle \sum_{m=1}^{M} I_U(r_1,\theta_1) \sum_{n=1}^{N} I_R(r_2,\theta_2) \right\rangle \\ &\quad = \left\langle \sum_{m=1}^{M} I_U(r_1,\theta_1) \right\rangle \left\langle \sum_{n=1}^{N} I_R(r_2,\theta_2) \right\rangle \\ &\qquad + \left| \sum_{m=1}^{M}\sum_{n=1}^{N} \Gamma_{U,R}(r_1,\theta_1;r_2,\theta_2) \right|^2, \end{aligned} \tag{3}$$

where, $\langle\cdot\rangle$ represents the ensemble average, $I_U(r_1,\theta_1)$ and $I_R(r_2,\theta_2)$ are the speckle intensities of vortex beams with topological charges l_U and l_R at the m-th and n-th angles, respectively. The first term in Eq. (3) is the intensity term, which serves only as a background term and does not affect the angle-averaged intensity cross-correlation function [46]. The second term is the cross-correlation function at M and N angles, with the angle-averaged intensity correlation function directly related to the second term. In the second term [49],

$$\begin{aligned} &\sum_{m=1}^{M}\sum_{n=1}^{N} \Gamma_{U,R}(r_1,\theta_1;r_2,\theta_2) \\ &\quad = \sum_{m=1}^{M}\sum_{n=1}^{N} \langle E_U(r_1,\theta_1) E_R^*(r_2,\theta_2)\rangle \\ &\qquad \times \gamma(r_1,\theta_1,r_2,\theta_2). \end{aligned} \tag{4}$$

At the $z = 0$ plane, the random phase with statistical distribution can generate a steady-state light source, which can be well described by the Gaussian-Schell correlator $\gamma(r_1,\theta_1,r_2,\theta_2)$ [46], expressed as

$$\gamma(r_1,\theta_1,r_2,\theta_2) = \exp\left[-\frac{r_1^2 + r_2^2 - 2r_1r_2\cos(\theta_1-\theta_2)}{{l_c}^2}\right], \tag{5}$$

where l_c is the coherence length. Without considering the aperture function, Eq. (4) can be expressed in terms of the angular spectrum as [46]

$$\begin{aligned} &\sum_{m=1}^{M}\sum_{n=1}^{N} \Gamma_{U,R}(\boldsymbol{k}_1,\boldsymbol{k}_2) \\ &\quad = \int\int\int\int \sum_{m=1}^{M}\sum_{n=1}^{N} \Gamma_{U,R}(r_1,\theta_1;r_2,\theta_2) \\ &\qquad \times \exp\begin{bmatrix} -\mathrm{i}\boldsymbol{k}_1 r_1\cos(\theta_1-\theta_k) \\ +\mathrm{i}\boldsymbol{k}_2 r_2\cos(\theta_2-\theta_k) \end{bmatrix} r_1 r_2 \mathrm{d}r_1\mathrm{d}r_2\mathrm{d}\theta_1\mathrm{d}\theta_2. \end{aligned} \tag{6}$$

When speckle pattern sets M and N contain patterns captured at approximately the same rotation angle of the scattering medium, the optical memory effect indicates that the resulting speckle fields retain a high degree of structural similarity [54–56]. Therefore, we assume that when spatial positions (r_1,θ_1) and (r_2,θ_2) nearly coincide, $r_1 \approx r_2$ and $\theta_1 \approx \theta_2$. Based on Eq. (5), it can be inferred that $\gamma(r_1,\theta_1,r_2,\theta_2) \approx 1$, indicating stronger spatial coherence between the two points. By setting $r_1 \approx r_2 = r'$ and $\theta_1 \approx \theta_2 = \theta'$, Eq. (6) becomes

$$\begin{aligned} &\sum_{m=1}^{M}\sum_{n=1}^{N} \Gamma_{U,R}(\boldsymbol{k},-\boldsymbol{k}) \\ &\quad = \iint \sum_{m=1}^{M}\sum_{n=1}^{N} a_U a_R \exp(\mathrm{i}\Delta l\theta') \\ &\qquad \times \exp[-2\mathrm{i}kr'\cos(\theta'-\theta_k)]\, r'^2 \mathrm{d}r'\mathrm{d}\theta', \end{aligned} \tag{7}$$

where $\boldsymbol{k}_1 = \boldsymbol{k}_2 = -\boldsymbol{k}$, $\Delta l = l_U - l_R$, and the angular part can be obtained using the Bessel function integral formula [17, 19]:

$$\int_0^{2\pi} \exp\left(\mathrm{i}\Delta l\theta\right) \exp(-2\mathrm{i}kr\cos\theta)\mathrm{d}\theta = 2\pi(-\mathrm{i})^{\Delta l} J_{\Delta l}(2kr), \tag{8}$$

combining Eq. (7) and Eq. (8), we can conclude that

$$\Gamma_{U,R} = 2A\pi(-\mathrm{i})^{\Delta l} \int a_U a_R J_{\Delta l}(2kr) r^2 \mathrm{d}r, \tag{9}$$

where A is the constant term. Assuming amplitudes a_U and a_R are those of an ideal PVB, whose width Δr is much smaller than the radius r_0 of the ring. Since the first maximum position of the Bessel function approximately satisfies $2kr \approx \Delta l + \beta \cdot \Delta l^{1/3} + \xi$, it determines the extremum position of the intensity distribution [17], β and ξ are coefficients introduced in the process of solving the extrema of Bessel functions, thereby forming a CCR with a certain radius. At a certain propagation position (Z), where Z is defined as the free-space distance from the exit surface of the medium to the camera detection plane after the PVB passes through the rotating scattering medium. The radius of the CCR can be expressed as

$$r_n = \delta \cdot \Delta l + \varepsilon \cdot \Delta l^{1/3} + \varsigma, \tag{10}$$

among them, δ, ε and ς are coefficients that vary with different Z. Based on the above relationship, it can be seen that when Z is fixed, if there are speckle patterns with nearly identical rotation angles in M and N, different Δl values will generate CCR of different radii, and the r_n is related to $\delta \cdot \Delta l + \varepsilon \cdot \Delta l^{1/3} + \varsigma$. Since the radius of the CCR is a non-negative real number, one can only extract the magnitude of Δl from this feature, while its sign remains undetermined; this further leads to the ability to only identify the magnitude of l_U without distinguishing its sign, ultimately making it impossible to determine the specific value of the OAM completely and unambiguously. Therefore, we propose a Dual-Reference PVB (DRPVB) method: At a certain distance Z, select $RPVB_1(l_{R1})$ and $RPVB_2(l_{R2})$, where $l_{R1} \neq l_{R2}$, observing the CCR radii $r_1 = \delta \cdot \Delta l_1 + \varepsilon \cdot \Delta {l_1}^{1/3} + \varsigma$ and $r_2 = \delta \cdot \Delta l_2 + \varepsilon \cdot \Delta {l_2}^{1/3} + \varsigma$, and $\Delta l_n = |l_U - l_{Rn}|$, we obtain candidate solution sets $L_1 = l_{R1} \pm \Delta l_1$ and $L_2 = l_{R2} \pm \Delta l_2$, and identify the measured l_U through $L_1 \cap L_2$.

Theoretical derivation indicates that satisfying Eq. (10) is predicated on the optical memory effect. However, when a vortex beam interacts with a rotating scattering medium, without a synchronous measurement strategy, it is difficult to capture speckle patterns at nearly identical rotation angles, leading to a large fraction of uncorrelated speckles. Therefore, to effectively obtain highly correlated speckles, we propose an NCCS algorithm. The principle is shown in Fig. 2. When unknown PVB and RPVB beams pass through a randomly rotating scattering medium, test and reference speckle libraries are collected at rotation angles $(\theta_1, \theta_2, \theta_p, \cdots, \theta_M)$ and $(\theta'_1, \theta'_2, \theta'_3, \cdots, \theta'_N)$, respectively. Subsequently, the NCCS algorithm is used to select highly correlated speckle sets from the two speckle libraries. At this point, the highly correlated speckle sets statistically correspond to samples with rotation angles within the optical memory range, ensuring at the data level that the approximate conditions in the theoretical derivation are satisfied. After averaging the selected highly correlated speckle patterns, the CCR with Δl mapping rules was obtained using the angular average intensity cross-correlation function.

To present the NCCS algorithm process, we first compute the cross-correlation matrix between speckles [49], denoted as

$$X_{\mathrm{corr}} = \mathcal{F}^{-1}\left[\mathcal{F}\left(I_U^p\right) \times \mathcal{F}^*\left(I_R^q\right)\right], \tag{11}$$

where I_U^p and I_R^q are the normalized speckle intensities with rotation angles θ_p and θ_q; $\mathcal{F}$ and $\mathcal{F}^{-1}$ represent the Fourier transform and inverse Fourier transform. Based on the cross-correlation matrix of the two images, the approximate position $(r_{\max}, \theta_{\max})$ of the maximum correlation value is initially coarsely located. However, discrete sampling imposes inherent limitations that fall short of the sub-pixel accuracy required for precise localization. Therefore, within the 3 × 3 neighborhood identified via coarse positioning, we perform quadratic surface fitting, as described by

$$P(r,\theta) = a + b\Delta r + c\Delta\theta + \mathrm{d}(\Delta r)^2 + e\Delta r\Delta\theta + f(\Delta\theta)^2, \tag{12}$$

where $\Delta r = r - r_{\max}, \Delta\theta = \theta - \theta_{\max}$, and a, b, c, d, e, and f are the coefficients of the terms. The sub-pixel offset is calculated as $(\mathrm{d}r, \mathrm{d}\theta)$ based on extreme values, and the peak position is adjusted to $(r_{\max} + \mathrm{d}r, \theta_{\max} + \mathrm{d}\theta)$. Finally, a high-precision NCCS is obtained based on the sub-pixel peak $X_{\mathrm{corr}}(r_{\max} + \mathrm{d}r, \theta_{\max} + \mathrm{d}\theta)$ and the standard deviations σ_{A} and σ_{B} of the two images, as follows:

$$NCCS = \frac{X_{\mathrm{corr}}(r_{\max} + \mathrm{d}r, \theta_{\max} + \mathrm{d}\theta)}{\sigma_A \cdot \sigma_B \cdot S}, \tag{13}$$

where S is the total number of pixels in the speckle image. When the NCCS value exceeds the threshold, the two speckle patterns are considered to be significantly correlated, thereby enabling the effective selection of highly correlated speckle pairs. Compared to the synchronous acquisition method proposed by Ma *et al.* [50], our approach accomplishes the identification of both the magnitude and the sign of the OAM without requiring any synchronization strategy, thus reducing system complexity while preserving accuracy.

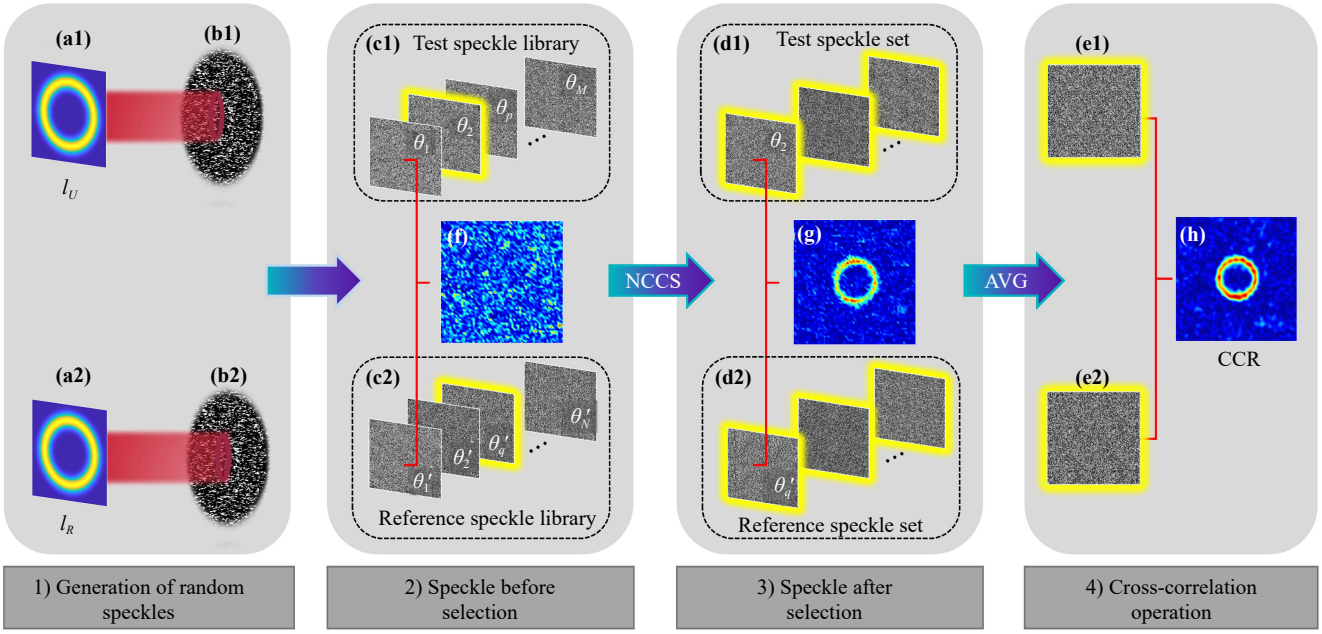

Fig. 2 Normalized cross-correlation screening (NCCS) algorithm. **(a1, a2)** Test PVB (l_U) and reference PVB (l_R). **(b1, b2)** Randomly rotated scattering medium. **(c1, c2)** Randomly collected simulated test and reference speckle libraries. (Yellow-outlined speckles indicate highly correlated speckles between the two libraries, while colorless-outlined speckles indicate uncorrelated speckles). **(d1, d2)** Test speckle set and reference speckle set (highly correlated speckles can be screened from the test and reference speckle libraries using the NCCS algorithm). **(e1, e2)** Averaged test speckle and averaged reference speckle obtained by superposition. **(f)** Speckles show low correlation with each other before selection and cannot map the CCR. **(g)** Speckles show high correlation with each other after selection and can map the CCR. **(h)** CCR based on the cross-correlation operation.

3 Simulation and analysis

In the simulation, the radii and widths of the test PVB and RPVB are both 2 mm and 0.5 mm. To realistically simulate the randomness of speckle acquisition during actual rotation, a random distribution function is used to generate a series of different discrete rotation angles $\theta_p = (0.1, 1.52, 2, \cdots)$ and $\theta_q = (0.53, 1.52, 2.54, \cdots)$. The scattering medium is modeled using a two-dimensional random phase screen, with its scattering characteristics characterized by two parameters: the standard deviation (σ) and the transverse correlation length (β) [57–59]. The simulation results are shown in Fig. 3. Among them, Figs. 3(a) and (b) are schematic diagrams of scattering media with two different roughness levels, corresponding to $\beta = 50\lambda, \sigma = \lambda$ and $\beta = 10\lambda, \sigma = \lambda$ respectively, both with a refractive index of 1.517. Figures 3(c1)–(c3) and (d1)–(d3) display the intensity distributions of the PVB under test (l_U sequentially as 1, 5, 10) and RPVB ($l_R = 1$), while (e1)–(e3) and (f1)–(f3) show their corresponding phase distributions. Figures 3(g1)–(g3) and (h1)–(h3) present the simulated speckle patterns of PVB and RPVB after NCCS screening and averaging under the roughness condition of $\beta = 50\lambda, \sigma = \lambda$; whereas Figs. 3(i1)–(j3) depict the corresponding simulation results for the roughness condition of $\beta = 10\lambda, \sigma = \lambda$. Figures 3(k1)–(l3) and (l1)–(l3) show the CCR obtained from the cross-correlation operation, which are $X_{\text{corr}}(l_1, l_1)$, $X_{\text{corr}}(l_5, l_1)$ and $X_{\text{corr}}(l_{10}, l_1)$ respectively. The above results indicate that under the same roughness conditions, different values of Δl lead to significant differences in the radius of the CCR, and the radius of the CCR is positively correlated with Δl. This positive correlation persists when the roughness varies, demonstrating that the proposed NCCS algorithm combined with the angular averaged intensity cross-correlation function maintains good applicability and robustness for rotating scattering media with varying roughness levels.

To investigate the CCR characteristics at different propagation distances (Z), we further analyzed the relationship between r_n and Δl, where $l_R = 1$ and Δl ranges from 1 to 16. The results are shown in Fig. 4. From Figs. 4(a1)–(a3), it can be observed that under the same roughness, CCR still persists with increasing Z. Based on the theoretical model derived from Eq. (10), the simulation data was subjected to nonlinear curve fitting using software, yielding a specific quantitative relationship between r_n and Δl. The detailed fitting method is provided in Supplement note 1. When Z is 50 mm, $r_n = 39.242\Delta l + 15.21\Delta l^{1/3} + 19.575$; at 60 mm, $r_n = 45.417\Delta l + 31.407\Delta l^{1/3} + 10.85$; and at 70 mm, $r_n = 47.828\Delta l + 82.484\Delta l^{1/3} - 33.949$. The results indicate that

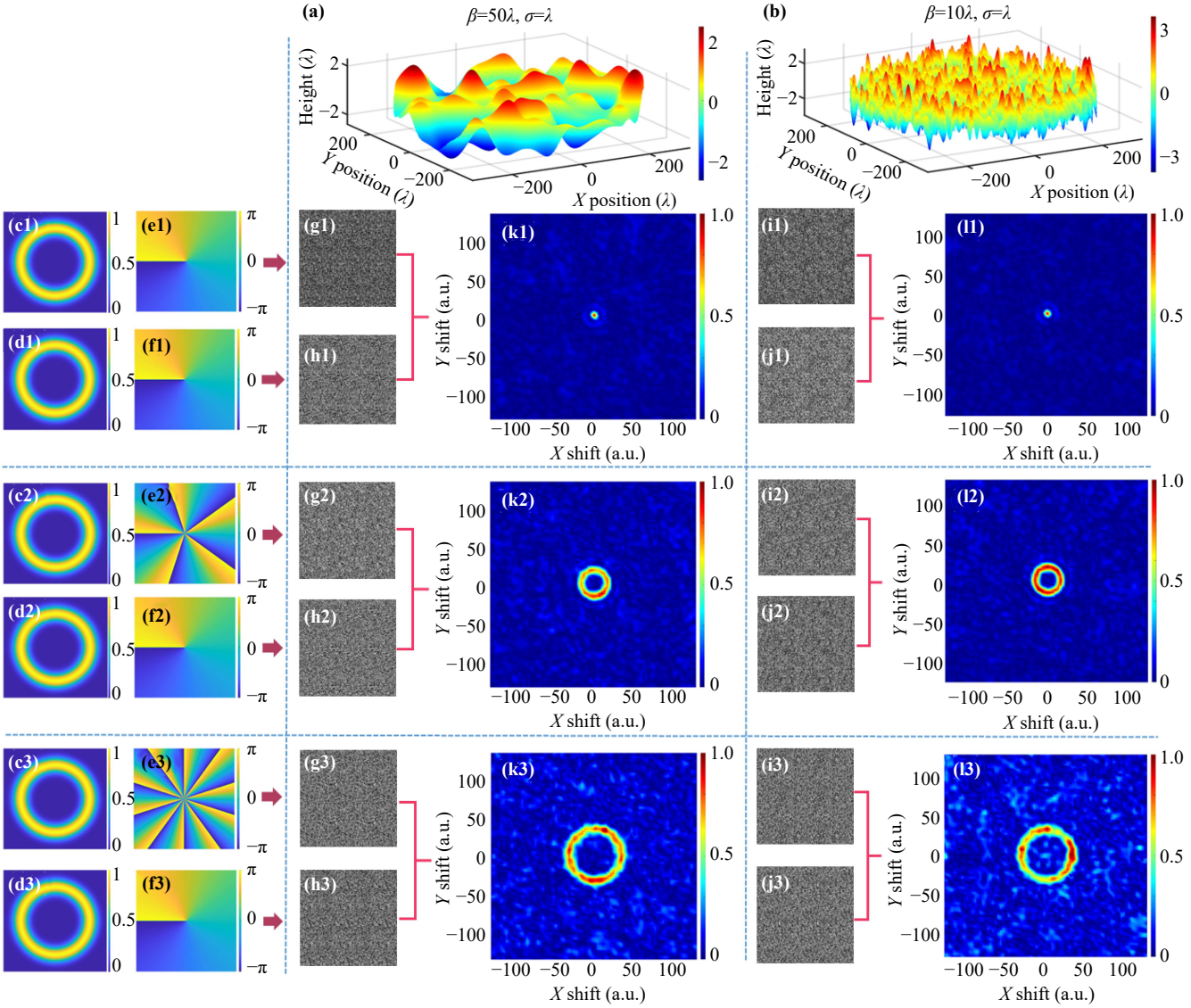

Fig. 3 Numerical simulation of the CCR for correlated speckle mapping under different topological charges and roughness conditions. **(a, b)** Roughness parameters are $\beta = 50\lambda, \sigma = \lambda$ and $\beta = 10\lambda, \sigma = \lambda$, respectively; **(c1–c3)** Intensity distribution of the test PVB (l_U: 1, 5, 10); **(d1–d3)** Intensity distribution of RPVB (l_R fixed at 1); **(e1–e3)** and **(f1–f3)** Phase distributions of PVB and RPVB, respectively; **(g1–g3)** and **(h1–h3)** Speckle simulation images of PVB and RPVB under condition $\beta = 50\lambda, \sigma = \lambda$; **(i1–i3)** and **(j1–j3)** Corresponding speckle simulation images under condition $\beta = 10\lambda, \sigma = \lambda$; **(k1–k3)** CCR obtained under condition $\beta = 50\lambda, \sigma = \lambda$; **(l1–l3)** CCR obtained under condition $\beta = 10\lambda, \sigma = \lambda$.

the positive correlation trend between r_n and Δl persists across different propagation distances, further validating the universality of the theoretical model.

Finally, we present a simulation analysis of the DRPVB method for recognizing unknown l_U, as shown in Fig. 5. Given a roughness of $\beta = 50\lambda, \sigma = \lambda$, and a tested topological charge $(l_U = 2)$, we select $RPVB_1\,(l_{R1} = 9)$ and $RPVB_2\,(l_{R2} = 15)$. At an observation distance of 50 mm, the CCR mapped based on Δl_n is obtained, as shown in Figs. 5(c1)–(c2). Calculating the radius of the CCR yields $r_1 = 323.2$ μm and $r_2 = 561.1$ μm. Combined with the relationship $r_n = 39.242\Delta l + 15.21\Delta l^{1/3} + 19.575$ of the CCR radius at 50 mm, this reveals $\Delta l_1 \approx 7$ and $\Delta l_2 \approx 13$. The corresponding topological charge candidate set is $L_1 = \{2, 16\}$ and $L_2 = \{2, 28\}$. By taking $L_1 \cap L_2$, the tested value is determined to be $l_U = 2$. Therefore, the size and sign of l_U can be determined based on the DRPVB method.

The simulation results above demonstrate that even without employing a synchronous acquisition strategy, the CCR characterizing OAM information can still be obtained under different propagation distances and roughness levels. Additionally, we have conducted a relevant exploration on the convenient relationship between r_n, Δl and Z in the Supplement note 2. The above analysis indicates that by combining the relationship between r_n

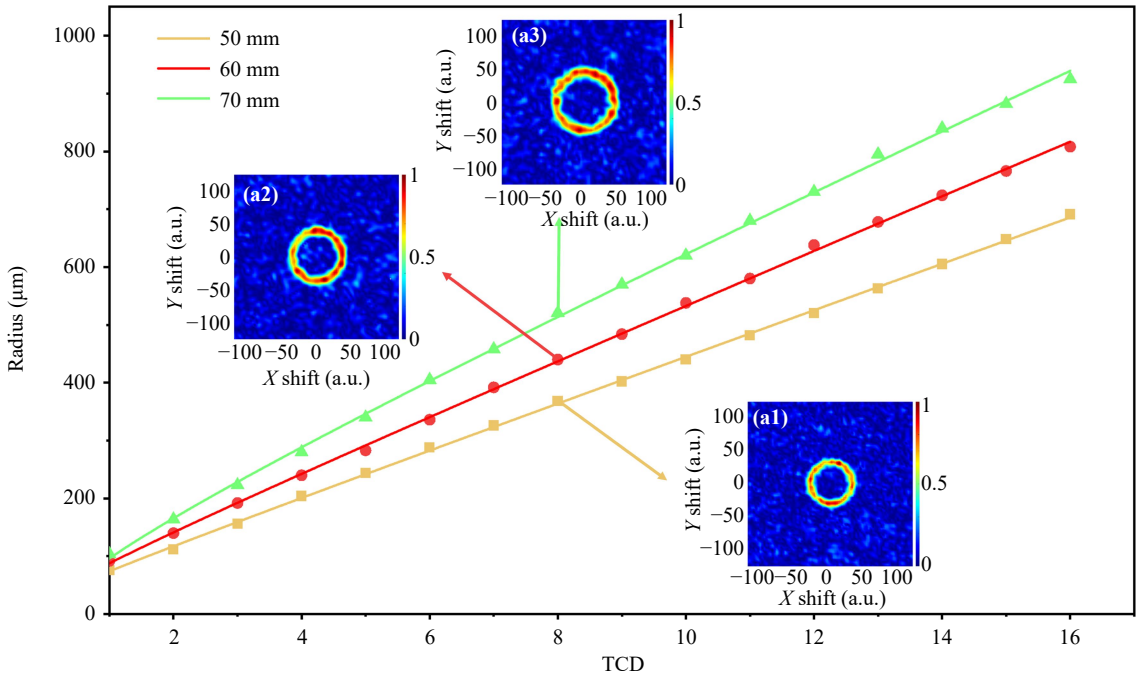

Fig. 4 Simulation analysis of CCR at different propagation distances. Under the conditions of roughness $\beta = 50\lambda, \sigma = \lambda$, a refractive index of 1.517, and $l_R = 1$, a radius of CCR varying with Δl (1–16) and Z (50 mm–70 mm). **(a1–a3)** show CCR at 50, 60, and 70 mm, with $\Delta l = 8$.

and Δl with the DRPVB method, the sorting and recognition of OAM mode.

4 Experimental validation

In the experiment, the hologram of the vortex beam was generated by a computer and loaded onto a spatial light modulator. The laser output (632.8 nm) was adjusted by a collimating beam expander and a polarizer before being incident on the spatial light modulator. The modulated beam underwent Fourier transformation through a 4f system to generate the desired vortex beam. The vortex beam forms speckles after passing through rotating ground glass diffusers (grit size of 120 and grit size of 220), which are then randomly captured by the camera, as shown in Fig. 6.

The radii and widths of PVB and RPVB were configured as 2 mm and 0.5 mm, respectively. The ground glass diffusers are uncoated on both sides, with a working wavelength of 400–700 nm, a refractive index of 1.517, and a thickness of 2 mm. The ground glass diffusers was rotated at a speed of 1 rpm, and the camera exposure time was 0.01 s. First, a series of speckles were randomly collected to form the test speckle library $(PVB\,(l_U))$. Then, two reference speckle pattern libraries $(RPVB_1\,(l_{R1}))$ and $(RPVB_2\,(l_{R2}))$ with different topological charges were randomly collected under consistent experimental conditions, with each library containing at least 5,000 speckle patterns.

First, we analyzed the correlation characteristics of speckle patterns at a propagation distance of 50 mm for different topological charges passing through scattering media with different roughness, as shown in Fig. 7. It can be seen that under different roughness and topological charge conditions, despite the interference from partial background noise, the CCR mapped by parameter Δl can all be effectively identified, and their variation trends remain consistent with the results of numerical simulations. In the experiment, we further analyzed issues such as NCCS analysis and threshold selection, slight offsets in the receiving position, and varying rotation speeds of the frosted glass, as detailed in Supplement Notes 3, 4, and 5. The results indicate that an appropriate threshold can effectively select highly correlated speckles, thereby enabling the extraction of CCR information. Even with minor receiving position deviations or rotational speed variations, the proposed method still efficiently extracts CCR information from highly correlated speckles.

Next, an experimental analysis of the CCR obtained at different propagation distances after $l_U = 10$ and $l_R = 1$ pass through rotating scattering media with different roughness is presented, as shown in Fig. 8. It can be observed that under different roughness conditions, the CCR can still be clearly identified at various distances. Although turntable vibration interference and stray light effects lead to enhanced background noise, the experimental results remain in good agreement with numerical simulations. In addition, we provide experi-

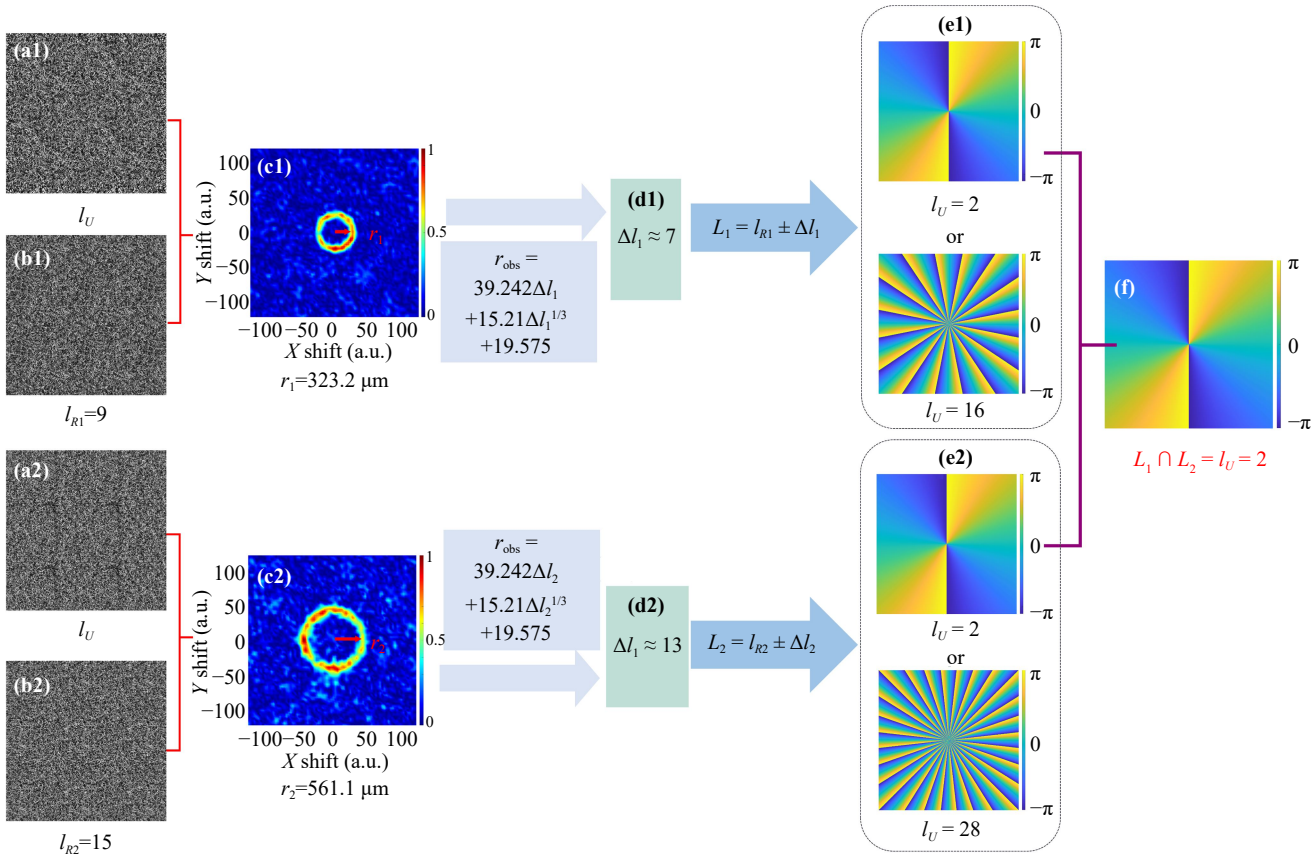

Fig. 5 Simulation analysis for recognizing l_U using the DRPVB method. At a roughness of $\beta = 50\lambda, \sigma = \lambda$, a refractive index of 1.517, and Z is 50 mm. **(a1, a2)** Average speckle simulation patterns of PVB (l_U) after NCCS selecting. **(b1, b2)** Average speckle simulation patterns of $RPVB_1\,(l_{R1} = 9)$ and $RPVB_2\,(l_{R2} = 15)$ after scattering and NCCS screening. **(c1, c2)** CCR mapped from Δl_1 and Δl_2, with radii $r_1 = 323.2$ μm and $r_2 = 561.1$ μm. **(d1, d2)** Topological charge differences $\Delta l_1 \approx 7$ and $\Delta l_2 \approx 13$. **(e1, e2)** Candidate sets $L_1 = \{l_U = 2, l_U = 16\}$ and $L_2 = \{l_U = 2, l_U = 28\}$ obtained from $l_{R1} \pm \Delta l_1$ and $l_{R2} \pm \Delta l_2$. **(f)** Result $l_U = 2$ obtained from candidate set $L_1 \cap L_2$.

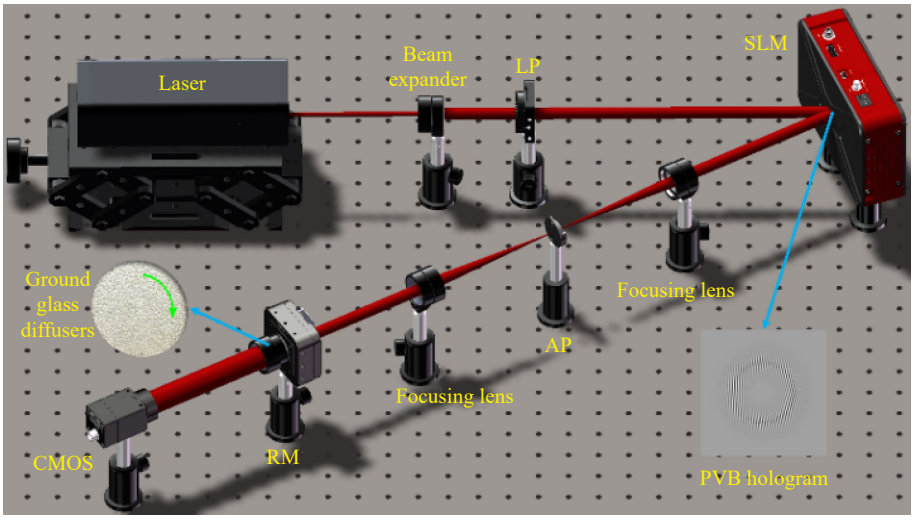

Fig. 6 Experimental layout: LP: Linear polarizer; SLM: Spatial light modulator; AP: Aperture diaphragm; RM: Rotary motor (including ground glass diffusers).

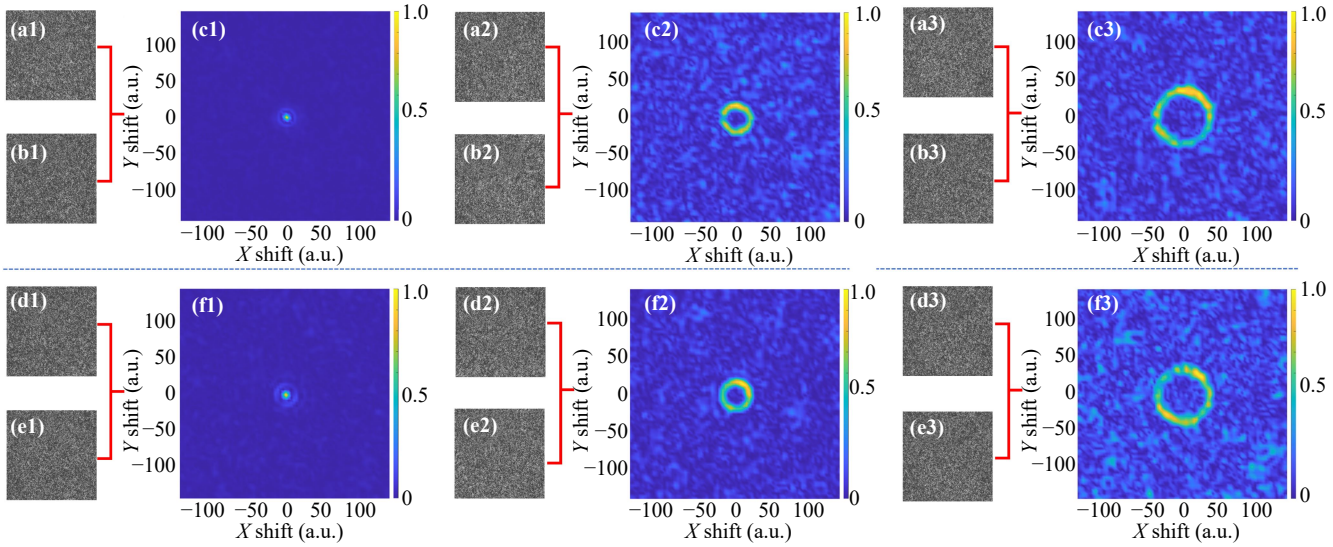

Fig. 7 Experimental analysis of CCR under different topological charges and roughness. Grit size of 220: **(a1–a3)** are the experimental speckle patterns obtained after NCCS and averaging processing, corresponding to $l_U = 1, 5$ and 10 respectively. **(b1–b3)** are processed experimental speckle patterns. l_R is consistently 1. **(c1–c3)** are the CCRs obtained based on speckle patterns, corresponding to $X_{\text{corr}}(l_1, l_1)$, $X_{\text{corr}}(l_5, l_1)$ and $X_{\text{corr}}(l_{10}, l_1)$ respectively. Grit size of 120: **(d1–d3)** are experimental speckle patterns, l_U is 1, 5, and 10, respectively. **(e1–e3)** are experimental speckle patterns, l_R is consistently 1. **(f1–f3)** are the CCR. $X_{\text{corr}}(l_1, l_1)$, $X_{\text{corr}}(l_5, l_1)$ and $X_{\text{corr}}(l_{10}, l_1)$.

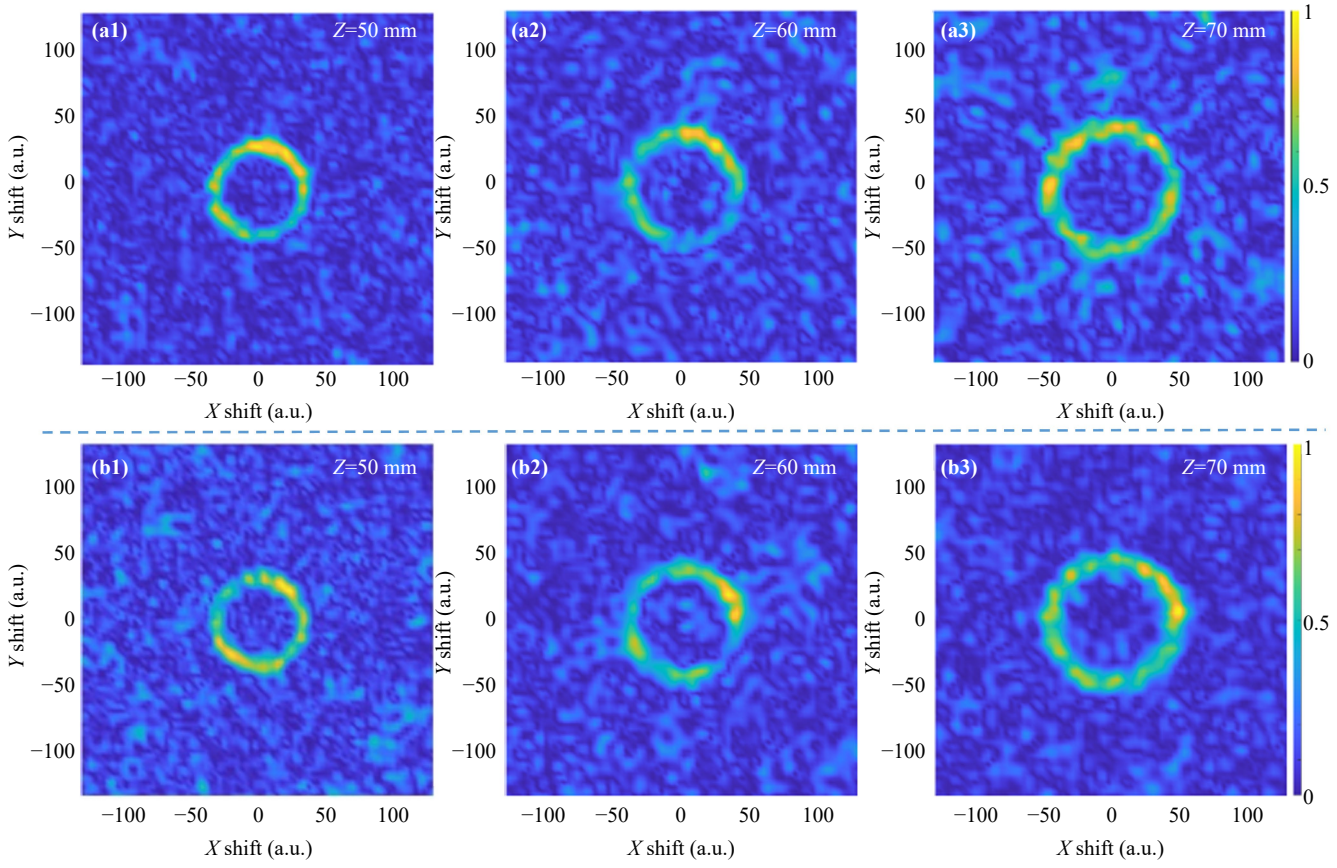

Fig. 8 Experimental analysis of CCR at different propagation distances. **(a1–a3)** For grit size of 220, CCR based on Δl mapping at 50, 60, and 70 mm for PVB ($l_U = 10$) and RPVB ($L_R = 1$) after passing through the scattering medium. **(b1–b3)** For grit size of 120, CCR based on Δl mapping at 50, 60, and 70 mm under the same conditions.

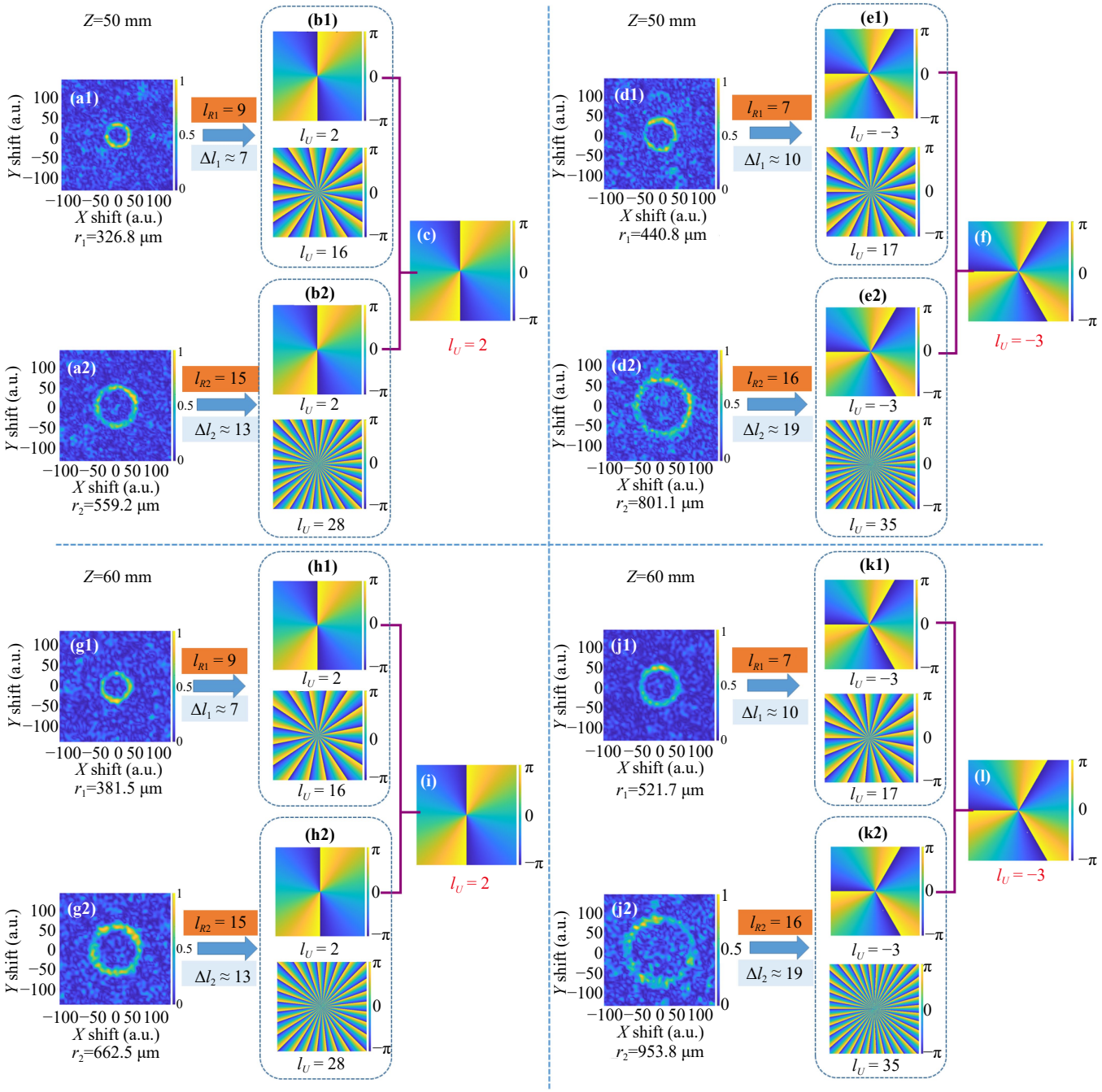

Fig. 9 Experimental analysis of recognizing l_U using the DRPVB method. **(a1, a2)** At 50 mm, the correlation radii mapped based on $\Delta l_1 = l_U - l_{R1}$ and $\Delta l_2 = l_U - l_{R2}$ are $r_1 = 326.8$ μm and $r_2 = 559.2$ μm. **(b1, b2)** Candidate sets $L_1 = \{l_U = 2, l_U = 16\}$ and $L_2 = \{l_U = 2, l_U = 28\}$ obtained based on $l_{R1} \pm \Delta l_1$ and $l_{R2} \pm \Delta l_2$. **(c)** The measured $l_U = 2$ derived based on $L_1 \cap L_2$. **(d1, d2)** $r_1 = 440.8$ μm and $r_2 = 801.1$ μm at 50 mm, where $l_{R1} = 7$ and $l_{R2} = 16$. **(e1, e2)** $L_1 = \{-3, 17\}$ and $L_2 = \{-3, 35\}$. **(f)** $l_U = -3$. **(g1, g2)** At 60 mm, $r_1 = 381.5$ μm and $r_2 = 662.5$ μm. **(h1, h2)** $L_1 = \{2, 16\}$ and $L_2 = \{2, 28\}$. **(i)** $l_U = 2$. **(j1, j2)** $r_1 = 521.7$ μm and $r_2 = 953.8$ μm at 60 mm. **(k1, k2)** $L_1 = \{-3, 17\}$ and $L_2 = \{-3, 35\}$, respectively. **(l)** $l_U = -3$.

mental analysis for longer propagation distances in Supplement note 6, demonstrating that the method can still effectively extract OAM information based on highly correlated speckles even at longer propagation distances.

Finally, experimental analyses of recognizing the unknown l_U using the DRPVB method are presented in Fig. 9. It can be observed that at an observation distance of 50 mm, by combining the relationship of $r_n = 39.242\Delta l + 15.21\Delta l^{1/3} + 19.575$, when l_U is 2, selecting $RPVB_1\,(l_{R1} = 9)$ and $RPVB_2\,(l_{R2} = 15)$ can identify $l_U = 2$, which is consistent with the simulation results.

Similarly, at a distance of 50 mm, when $l_U = -3$, selecting $RPVB_1\,(l_{R1} = 7)$ and $RPVB_2\,(l_{R2} = 16)$ can identify $r_1 = 440.8$ μm and $r_2 = 801.1$ μm, accurately identify $l_U = -3$. When the observation distance is 60 mm, by combining the relationship of $r_n = 45.417\Delta l + 31.407\Delta l^{1/3} + 10.85$, l_U can still be accurately identified.

The experimental results presented above demonstrate that, even without relying on synchronous speckle acquisition strategies, it is still possible to obtain CCR that characterizes OAM, and these results are in good agreement with numerical simulations. This demonstrates that by combining the CCR radius feature with the DRPVB method, effective sorting and recognition of OAM can be achieved.

5 Discussion and conclusion

In summary, we propose and demonstrate the sorting and recognition of OAM of a vortex beam after passing through rotating scattering media. By constructing a speckle correlation model under rotating scattering media, a mapping relationship between topological charge differences and CCR characteristics is established, and the dual-reference PVB method is utilized to achieve the sorting and recognition of unknown topological charges. Both simulations and experiments confirm that processing randomly acquired speckle pattern sets using the NCCS algorithm and angular average intensity cross-correlation function can effectively extract CCR containing OAM information. On this basis, only two reference beams with different topological charges are needed to achieve complete identification of an unknown topological charge. This method overcomes the technical limitations associated with synchronous acquisition in dynamic scattering media and enables the effective discrimination of both the sign and magnitude of OAM. It is worth noting that pre-determining the propagation distance is a prerequisite for achieving quantitative recognition. Exploring and establishing a more universal and convenient calibration relationship between the CCR radius, propagation distance, and topological charge difference is the key to promoting the broader application of this method. With the continuous growth of information dimensions and data volume in optical imaging and communication systems, this OAM sorting and recognition method provides a reference for subsequent multi-OAM recognition and promotes the in-depth investigation and engineering application of vortex beam communication and information transmission.

Declarations The authors declare that they have no competing interests and there are no conflicts.

Electronic supplementary materials The online version contains supplementary material available at https://doi.org/10.15302/frontphys.2026.102202.

Acknowledgements This work was supported by the National Natural Science Foundation of China (Grant Nos. 62173342, 61805283, and 62203466).

References

1. Z. Wan, Y. Shen, Z. Wang, Z. Shi, Q. Liu, and X. Fu, Divergence-degenerate spatial multiplexing towards future ultrahigh capacity, low error-rate optical communications, *Light Sci. Appl.* 11(1), 144 (2022)
2. H. Xu, J. Chen, B. Wang, H. Li, C. Song, Q. Tan, Z. Zhao, W. Liu, L. Shi, J. Li, and J. Yao, Non-local metasurface generates highly efficient transmission vortex by intrinsic singularity and generalized Kerker effect, *PhotoniX* 6(1), 8 (2025)
3. Y. Bai, H. Lv, X. Fu, and Y. Yang, Vortex beam: generation and detection of orbital angular momentum, *Chin. Opt. Lett.* 20(1), 012601 (2022)
4. X. Meng, Y. Hu, C. Wan, and Q. Zhan, Optical vortex fields with an arbitrary orbital angular momentum orientation, *Opt. Lett.* 47(17), 4568 (2022)
5. S. Fu, Y. Zhai, J. Zhang, X. Liu, R. Song, H. Zhou, and C. Gao, Universal orbital angular momentum spectrum analyzer for beams, *PhotoniX* 1(1), 19 (2020)
6. A. E. Willner, H. Song, K. Zou, H. Zhou, and X. Su, Orbital angular momentum beams for high-capacity communications, *J. Lightwave Technol.* 41(7), 1918 (2023)
7. Y. Zheng, Y. Li, F. Wang, R. Liu, D. Deng, Y. Cai, and Y. Zhao, Precision measurement of the topological charge of a fractional vortex beam based on angular-grating-diffraction OAM spectrum, *Opt. Express* 33(1), 553 (2025)
8. H. Yan, Y. Fan, Z. Huang, R. Tang, S. Ma, Y. Lei, Y. Ding, X. Zhu, T. Liu, Z. Liu, and Y. Ren, Coherent detection of the rotational Doppler effect measurement based on triple Fourier transform, *Opt. Express* 32(7), 11873 (2024)
9. H. Zhou, D. Fu, J. Dong, P. Zhang, and X. Zhang, Theoretical analysis and experimental verification on optical rotational Doppler effect, *Opt. Express* 24(9), 10050 (2016)
10. T. Yu, H. Xia, W. Xie, and Y. Peng, Orbital angular momentum mode detection of the combined vortex beam generated by coherent combining technology, *Opt. Express* 28(24), 35795 (2020)
11. I. M. Vellekoop, and A. P. Mosk, Focusing coherent light through opaque strongly scattering media, *Opt. Lett.* 32(16), 2309 (2007)
12. J. Shi, X. Zhu, F. Yang, S. Wang, K. Li, P. Niu, J. Yao, L. Tang, and X. Yang, All-dielectric integrated OAM meta-antenna in the 6G terahertz communication window, *Front. Phys. (Beijing)* 21, 095204 (2026)
13. W. Yang and G. Situ, Recovery of the topological charge of a vortex beam propagated through a scattering layer, *Appl. Opt.* 60(10), B95 (2021)
14. L. Chen, Quantum discord of thermal two-photon orbital angular momentum state: Mimicking teleportation to transmit an image, *Light Sci. Appl.* 10(1), 148 (2021)
15. Z. C. Ren, L. Fan, Z. M. Cheng, Z. F. Liu, Y. C. Lou,

S. Y. Huang, C. Chen, Y. Li, C. Tu, J. Ding, X. L. Wang, and H. T. Wang, On-demand orbital angular momentum comb from a digital laser, *Optica* 11(7), 951 (2024)
16. J. Leach, B. Jack, J. Romero, A. K. Jha, A. M. Yao, S. Franke-Arnold, D. G. Ireland, R. W. Boyd, S. M. Barnett, and M. J. Padgett, Quantum Correlations in Optical Angle–Orbital Angular Momentum Variables, *Science* 329(5992), 662 (2010)
17. M. Abramowitz, Handbook of Mathematical Functions with Formulas, Graphs, and Mathematical Tables, p. 1076 (1972)
18. M. Chen, M. Mazilu, Y. Arita, E. M. Wright, and K. Dholakia, Dynamics of microparticles trapped in a perfect vortex beam, *Opt. Lett.* 38(22), 4919 (2013)
19. J. García-García, C. Rickenstorff-Parrao, R. Ramos-García, V. Arrizón, and A. S. Ostrovsky, Simple technique for generating the perfect optical vortex, *Opt. Lett.* 39(18), 5305 (2014)
20. J. Wang, J. Liu, S. Li, Y. Zhao, J. Du, and L. Zhu, Orbital angular momentum and beyond in free-space optical communications, *Nanophotonics* 11(4), 645 (2021)
21. A. E. Willner, K. Pang, H. Song, K. Zou, and H. Zhou, Orbital angular momentum of light for communications, *Appl. Phys. Rev.* 8(4), 041312 (2021)
22. S. Chen, J. Chen, T. Xia, Z. Xie, Z. Huang, H. Zhou, J. Liu, Y. Chen, Y. Li, S. Yu, D. Fan, and X. J. Yuan, Optical vortices in communication systems: Mode (de)modulation, processing, and transmission, *Adv. Photonics* 7(4), 044001 (2025)
23. J. Zhou, Y. Yin, J. Tang, Y. Xia, and J. Yin, Information transmission through parallel multi-task-based recognition of high-resolution multiplexed orbital angular momentum, *Front. Phys. (Beijing)* 19, 52202 (2024)
24. H. Di Lorenzo Pires, H. C. B. Florijn, and M. P. van Exter, Measurement of the spiral spectrum of entangled two-photon states, *Phys. Rev. Lett.* 104(2), 020505 (2010)
25. M. Malik, S. Murugkar, J. Leach, and R. W. Boyd, Measurement of the orbital-angular-momentum spectrum of fields with partial angular coherence using double-angular-slit interference, *Phys. Rev. A* 86(6), 063806 (2012)
26. I. A. Litvin, A. Dudley, F. S. Roux, and A. Forbes, Azimuthal decomposition with digital holograms, *Opt. Express* 20(10), 10996 (2012)
27. G. Gibson, J. Courtial, M. J. Padgett, M. Vasnetsov, V. Pas'ko, S. M. Barnett, and S. Franke-Arnold, Free-space information transfer using light beams carrying orbital angular momentum, *Opt. Express* 12(22), 5448 (2004)
28. N. K. Fontaine, R. Ryf, H. Chen, D. T. Neilson, K. Kim, and J. Carpenter, Laguerre-Gaussian mode sorter, *Nat. Commun.* 10(1), 1865 (2019)
29. H. Kupianskyi, S. A. R. Horsley, and D. B. Phillips, High-dimensional spatial mode sorting and optical circuit design using multi-plane light conversion, *APL Photonics* 8(2), 026101 (2023)
30. Z. Lin, Y. Wen, Y. Chen, and S. Yu, Transmissive multi-plane light conversion for demultiplexing orbital angular momentum modes, in: *Conference on Lasers and Electro-Optics*, pp 1–2 (2020)
31. J. Zhang, Z. Ye, J. Yin, L. Lang, and S. Jiao, Polarized deep diffractive neural network for sorting, generation, multiplexing, and de-multiplexing of orbital angular momentum modes, *Opt. Express* 30(15), 26728 (2022)
32. Q. Jia, Y. Zhang, B. Shi, H. Li, X. Li, R. Feng, F. Sun, Y. Cao, J. Wang, C. W. Qiu, and W. Ding, Vector vortex beams sorting of 120 modes in visible spectrum, *Nanophotonics* 12(20), 3955 (2023)
33. Y. Shi, Z. Ma, H. Chen, Y. Ke, Y. Chen, and X. Zhou. High-resolution recognition of FOAM modes via an improved EfficientNet V2 based convolutional neural network, *Front. Phys. (Beijing)* 19, 32205 (2024)
34. S. G. Reddy, S. Prabhakar, A. Kumar, J. Banerji, and R. P. Singh, Higher order optical vortices and formation of speckles, *Opt. Lett.* 39(15), 4364 (2014)
35. L. Gong, Q. Zhao, H. Zhang, X. Y. Hu, K. Huang, J. M. Yang, and Y. M. Li, Optical orbital-angular-momentum-multiplexed data transmission under high scattering, *Light Sci. Appl.* 8(1), 27 (2019)
36. Z. Liu, H. Zhang, K. Liu, B. Zhang, X. Fu, and Q. Liu, Data transmission under high scattering based on OAM-basis transmission matrix, *Opt. Lett.* 47(17), 4580 (2022)
37. K. Lee and Y. Park, Exploiting the speckle-correlation scattering matrix for a compact reference-free holographic image sensor, *Nat. Commun.* 7(1), 13359 (2016)
38. H. Zhang, B. Zhang, and Q. Liu, OAM-basis transmission matrix in optics: a novel approach to manipulate light propagation through scattering media, *Opt. Express* 28(10), 15006 (2020)
39. Q. Zhao, P. P. Yu, Y. F. Liu, Z. Q. Wang, Y. M. Li, and L. Gong, Light field imaging through a single multimode fiber for OAM-multiplexed data transmission, *Appl. Phys. Lett.* 116(18), 181101 (2020)
40. F. Feng, J. Hu, Z. Guo, J. A. Gan, P. F. Chen, G. Chen, C. Min, X. Yuan, and M. Somekh, Deep learning-enabled orbital angular momentum-based information encryption transmission, *ACS Photonics* 9(3), 820 (2022)
41. Y. Liu, Z. Zhang, P. Yu, Y. Wu, Z. Wang, Y. Li, W. Liu, and L. Gong, Learning-enabled recovering scattered data from twisted light transmitted through a long standard multimode fiber, *Appl. Phys. Lett.* 120(13), 131101 (2022)
42. P. S. Badavath, V. Raskatla, T. P. Chakravarthy, and V. Kumar, Speckle-based structured light shift-keying for non-line-of-sight optical communication, *Appl. Opt.* 62(23), G53 (2023)
43. V. Raskatla, P. S. Badavath, and V. Kumar, Speckle-learned convolutional neural network for the recognition of intensity degenerate orbital angular momentum modes, *Opt. Eng.* 62(3), 036104 (2023)
44. J. Liu, P. Wang, X. Zhang, Y. He, X. Zhou, H. Ye, Y. Li, S. Xu, S. Chen, and D. Fan, Deep learning based atmospheric turbulence compensation for orbital angular momentum beam distortion and communication, *Opt. Express* 27(12), 16671 (2019)
45. A. Kumar, J. Banerji, and R. P. Singh, Hanbury Brown–Twiss-type experiments with optical vortices

and observation of modulated intensity correlation on scattering from rotating ground glass, *Phys. Rev. A* 86(1), 013825 (2012)
46. A. J. Jesus-Silva, J. M. Hickmann, and E. J. S. Fonseca, Strong correlations between incoherent vortices, *Opt. Express* 20(18), 19708 (2012)
47. C. R. Alves, A. J. Jesus-Silva, and E. J. S. Fonseca, Characterizing coherence vortices through geometry, *Opt. Lett.* 40(12), 2747 (2015)
48. Vinu R. V and R. K. Singh, Determining helicity and topological structure of coherent vortex beam from laser speckle, *Appl. Phys. Lett.* 109, 111108 (2016)
49. R. Ma, K. Luo, S. Pokharel, Z. Wang, O. Korotkova, J. He, W. Zhang, D. Fan, A. Gomes, and J. Liu, Orbital-angular-momentum-dependent speckles for spatial mode sorting and demultiplexing, *Optica* 11(5), 595 (2024)
50. R. Ma, C. K. Wang, O. Korotkova, J. S. He, W. L. Zhang, Z. H. Zhu, D. Y. Fan, and J. Liu, Orbital-angular-momentum-mediated information extraction from dynamic scattering, *Laser Photonics Rev.* 20(3), e00978 (2025)
51. W. Ren, H. Zhang, X. Mao, D. Xu, Z. Lu, W. Lin, S. Duan, and B. Liu, Deep-learning-assisted orbital angular momentum mode recovery under atmospheric turbulence for free-space optical communication, *J. Lightwave Technol.* 43(18), 8647 (2025)
52. G. M. Balasubramaniam, R. Kumar, and S. Arnon, Vortex beams and deep learning for optical wireless communication through turbulent and diffuse media, *J. Lightwave Technol.* 42(10), 3631 (2024)
53. W. Xiong, P. Wang, M. Cheng, J. Liu, Y. He, X. Zhou, J. Xiao, Y. Li, S. Chen, and D. Fan, Convolutional neural network based atmospheric turbulence compensation for optical orbital angular momentum multiplexing, *J. Lightwave Technol.* 38(7), 1712 (2020)
54. H. Liu, Z. Liu, M. Chen, S. Han, and L. V. Wang, Physical picture of the optical memory effect, *Photon. Res.* 7(11), 1323 (2019)
55. G. Osnabrugge, R. Horstmeyer, I. N. Papadopoulos, B. Judkewitz, and I. M. Vellekoop, Generalized optical memory effect, *Optica* 4(8), 886 (2017)
56. H. Yılmaz, M. Kühmayer, C. W. Hsu, S. Rotter, and H. Cao, Customizing the angular memory effect for scattering media, *Phys. Rev. X* 11(3), 031010 (2021)
57. Y. Zhai, J. Fan, H. Qiao, T. Zhou, J. Wu, and Q. Dai, The rotational Doppler effect of twisted photons in scattered fields, *Laser Photonics Rev.* 17(10), 2201022 (2023)
58. T. R. Thomas, Rough Surfaces, 2nd Ed., Imperial College Press, 1999
59. C. Cui, Z. Wang, X. Zhan, J. Wang, L. Liu, Z. Li, and C. J. A. O. Wu, Measurement of the adjustable slight roughness emulated by a spatial light modulator employing the vortex beam speckle pattern, *Appl. Opt.* 59(12), 3630 (2020)